Ternary Mixed Nickel Cobalt Iron Oxide Nanorods as a High-Performance Asymmetric Supercapacitor Electrode

Alaa Y Faid [1, *] and Hadeer Ismail [2]

[1] Materials Science and Engineering department, Norwegian University of Science and Technology, Norway

[2] Faculty of Engineering, Cairo University, Egypt

*Correspondence: alaa.faid@ntnu.no; Tel.: +47-46238951

Abstract: By utilizing a facile microwave process, ternary nickel cobalt iron oxide ($NiCoFeO_4$) nanorods were synthesized. A comprehensive investigation of morphological, structural and surface chemistry of the nanorods have been carried out. The electrochemical investigation of $NiCoFeO_4$ nanorods shows superior supercapacitive characteristics achieving a maximum specific capacitance (C_{sp}) of 1263 F/g at a current density of 1 A/g and cyclic stability retaining 97.2 % of capacitance after 2000 cycles. Asymmetric supercapacitor based on $NiCoFeO_4$ nanorods displays a high-power density of 10 kW/kg, energy density of 32 W h/ kg, coulombic efficiency of 95.5% and capacitance retention of 94% after 4000 cycles. The asymmetric supercapacitor is featuring an outstanding potential for practical supercapacitors due to high surface area nanorod morphology and mixed transition metal oxide synergetic effect.

Keywords: nanorods; ternary oxide; microwave; supercapacitors.

Introduction

Supercapacitors represent prominent devices for energy storage applications for its enormous power density and excellent cycling stability.[1,2] Therefore, it is crucial to explore new materials for supercapacitors electrodes that meet the requirements of high-power density and long durability for industrial energy firms.[3] Supercapacitors can be classified according to the energy storage mechanism into two types: electrochemical double layer capacitor with carbon electrodes,[4] and pseudo-capacitors with transition metal oxides or conducting polymers electrode [5]. Transition metal oxides such as NiO, Co_3O_4, Fe_2O_3, MnO_2, V_2O_5 and spinel oxides employ fast and reversible faradaic redox reactions (pseudo-capacitance) that involve ions and electrons in their charge storage mechanism.[6,7]

Spinel nickel ferrites are fascinating due to their impressive magnetic, electrochemical, electrical properties abundant redox states, high theoretical specific capacitance, low cost, environmental benignity[8], and electrochemical stability.[9,10,11,12] Subsequently, several studies have been performed on supercapacitor electrode materials based on ferrite oxide that offers multiple redox reactions, including contributions from both M and Fe ions. [13,12,14,15,16,17] Spinel nickel cobaltite ($NiCo_2O_4$) exhibits improved electrical conductivity and electrochemical activity.[18] These advantages drive it to be a more promising and scalable alternative electrode material for high-performance supercapacitors applications.[19] $NiCo_2O_4$ benefitted from the synergy effects between Ni and cobalt ions demonstrates improved redox reactions and endorsed structural variations.[20] However mixed ternary transition metal ferrites, $ABFe_2O_4$, (where A and B consist of a combination of Cu, Co or Ni) have not been explored in details as a potential candidate for supercapacitors.

Nanostructured supercapacitor electrodes show enhanced kinetics and activity due to higher specific surface area (SSA), and shorter pathways for electron and ion transport in comparison with their bulk counterparts.[21,22] Therefore, development of nanostructured Transition metal oxides (TMOs) with high SSA morphology provides a promising candidate for supercapacitor applications. The microwave-assisted process (MAP) is a simple and useful technique.[23,24,25] MAP process is environmentally friendly for its efficient reactant-microwave energy interaction than in the conventional heating method. [26] Many transition metal oxides/hydroxides such as α-$Ni(OH)_2$, NiO, Co_3O_4, and Fe_3O_4 with various morphologies have been synthesized by the MAH method.[27,28,29,26]

Therefore, synthesis and characterization of $NiCoFeO_4$ nanorods as potential supercapacitor electrode materials. $NiCoFeO_4$ can be a promising and cheap alternative for supercapacitors electrode. Herein, we report a facile MAH synthetic strategy for the preparation of ternary oxide nanorods. $NiCoFeO_4$ nanorods with a well-conserved morphology have been fabricated. The $NiCoFeO_4$ nanorods acting as electrode materials for supercapacitors exhibit a high specific capacitance and remarkable electrochemical stability. The excellent performance benefits from the superiority of the hierarchically porous nanorods, convenient ion transport within and between the nanorods and rich redox states of $NiCoFeO_4$.

Experimental Work :

Synthesis of nanowires:

In a typical fabrication procedure, 3 mmol $Fe(NO_3)_3{\cdot}9H_2O$ (ACS reagent, ≥98%, Sigma-Aldrich) , 6 mmol $Co(NO_3)_2{\cdot}6H_2O$ (reagent grade, 98%, Sigma-Aldrich), 3 mmol $Ni(NO_3)_2{\cdot}6H_2O$ (purum p.a., crystallized, ≥97.0%, Sigma-Aldrich), 4 mmol NH_4F (ACS reagent, ≥98.0%, Sigma-Aldrich), and 12 mmol $C(NH_2)_2$ (powder, Sigma-Aldrich) were mixed with 70 mL of Milli Q water (18 m ohm)at room temperature and stirred for 30 min. The resulted solution was transferred to a microwave oven (Monowave 400, Anton-Paar) at 750 W, 80 ℃ for 10 min. The produced precipitate was washed repeatedly with Milli Q water and isopropanol. Then the precipitate was vacuum dried at 60 ℃, overnight and annealed at 400 ℃ in argon gas for 2 h to obtain $NiCoFeO_4$ nanorods.

Structural and Morphological Characterization

The morphologies and microstructures of $NiCoFeO_4$ nanorods were observed using a field emission scanning electron microscope (FESEM, Hitachi S-4800). Elemental composition was identified by means of energy dispersive X-ray spectroscopy (EDX) within Hitachi S-4800. Phases and structural characteristics presented in $NiCoFeO_4$ nanorods were carried out via a PANalytical X'pert PRO X-ray diffraction (XRD) device which employs a Cu Kα radiation. Transmission electron microscopy (TEM) was used for further in-depth structural characterization using a (JEOL JEM-2100) device. TEM was operating at an accelerated voltage of 200 keV. TEM sample of $NiCoFeO_4$ nanorods was dispersed in ethanol and then a drop of solution was deposited on a carbon-coated copper grid and dried at room temperature. Raman spectrum was recorded on a dispersive Raman microprobe (Pro Raman-L Analyzer) using an excitation wavelength of 532 nm. X-ray photoelectron spectroscopy (XPS) is employed to investigate surface chemistry of $NiCoFeO_4$ nanorods using a Thermo Scientific ESCALAB-250Xi spectrometer microprobe with a monochromatic micro-focused Al-K_α radiation. The adsorption and specific surface area were characterized using a Quantachrome NOVA Station device by Brunauer– Emmett–Teller (BET) analysis of N_2 gas adsorption/desorption isotherms at 77 K.

Electrochemical Measurements

A homogenous and uniform slurry of $NiCoFeO_4$ nanorods with carbon black (conductive additive), polyvinylidene difluoride (binder), dimethylformamide (DMF) (solvent) with a weight ratio of 70: 20: 10 used as a working electrode. The prepared slurry was stirred at 750 rpm for 24 h at 22 °C. The slurry was coated on a 1 cm^2 nickel foam (support and current collector) and dried at 60 °C. Nickel foam was cleaned in a 3 M HCl solution for 15 min to remove NiO surface layer subsequently the nickel foam rinsed in deionized water and ethanol. The mass loading of $NiCoFeO_4$ nanorods was kept 2 ± 0.5 mg/cm^2. Three-electrode cell consists of the working electrode as indicated above, Pt foil (counter electrode), and saturated calomel electrode (SCE) (reference electrode) in 6 M KOH solution at 22 °C were used to investigate the supercapacitive performance of the prepared $NiCoFeO_4$ nanorods electrode. Electrochemical characterization methods such as galvanostatic charging/discharging (GCD), cyclic voltammetry (CV), and impedance spectroscopy (EIS) were carried out using (CHI 760D, CH Instruments, U.S.A.) workstation. CV characterization was carried out within 0–0.45 V potential range at different scan rates (5 to 100 mV/sec). GCD measurements were done at various current densities (1–11 A/g) within the same range of potential. EIS measurements were carried out in 100 kHz to 0.1 Hz frequency range at open circuit potential with a 10 mV sinusoidal perturbation amplitude. The specific capacitance (C_{sp}, F/g) was calculated according to the following equation from CV and GCD measurements:[30]

$$C_{sp} = \frac{\int I\, dv}{mv\Delta V} = \frac{I\,\Delta t}{m\Delta V} \qquad \textit{Equation 1}$$

where I is current (A), m is the active material mass (g), v is the scan rate (mV/sec), ΔV is the potential range (V), and Δt is the time of discharge (s).

Coulombic efficiency (η) was calculated from GCD measurements as follows:

$$\eta = \frac{t_d}{t_c} \times 100 \quad \textit{Equation 2}$$

where t_d and t_c are the time of discharging and charging, respectively.

Fabrication of asymmetric supercapacitor

To test the validation of $NiCoFeO_4$ nanorods as a high-performance supercapacitors electrode in a realistic application, an asymmetric supercapacitor was fabricated from our prepared material. $NiCoFeO_4$ nanorods on nickel foam act as the positive electrode, activated carbon (AC) as the negative electrode, a piece of filter paper as a separator and 6.0 M KOH as an electrolyte. The AC-based negative electrode was fabricated from a homogenous slurry of AC (70%), carbon black (20%) and poly(vinylidene difluoride) (10%) in N, N-dimethylformamide as a solvent. Then, the slurry was applied as a coating onto Ni foam current collector and dried for 24 h at 40 °C. To balance the stored charge on electrodes (Q), the mass loading ratios of the electroactive materials on both positive and negative electrodes should be balanced according to the following equation:[31]

$$m_+ \times \Delta V_+ \times C_{sp+} = m_- \times \Delta V_- \times C_{sp-} \quad \textit{Equation 3}$$

where m is the active material mass (g), C_{sp} is the specific capacitance (F/g), and ΔV is the potential range for charge/discharge process for the positive (+) and negative (−) electrodes, respectively.

The energy density E_d and the power density P_d of the $NiCoFeO_4$ supercapacitor can be calculated from Eq (4), (5) and (6): [32]

$$E = \frac{1}{2} C_{sp}\, \Delta V \quad \textit{Equation 4}$$

Eq (4) can be reformed as follows:[32]

$$E = \frac{1}{2} \frac{I\, \Delta V\, t}{m} \quad \textit{Equation 5}$$

$$P = \frac{E}{t} \quad \textit{Equation 6}$$

where I is the current (A), m is the active material mass (kg), ΔV is the potential range (V), and t is the discharge time.

Results and discussions

Structural Characterization

Figure 1. a and 1.b show typical SEM images of $NiCoFeO_4$ nanorods. $NiCoFeO_4$ nanorods have a diameter ranging ca. 150-200 nm with porous morphology along the length of the nanorod. Further characterization of nanorod structure has been carried out using low and high magnification TEM. Figure 1.c show the HR-TEM images of the $NiCoFeO_4$ nanorods confirming the formation of nanorod morphology with porosity along the rod axis. TEM (Figure 1.d) indicated that the nanorods consist of nanoparticles. The selected area electron diffraction (SAED) pattern of $NiCoFeO_4$ nanorods in Figure 1.e shows continuous diffraction rings corresponding to the existence of crystalline planes due to the polycrystalline nature in the nanorods. [33]

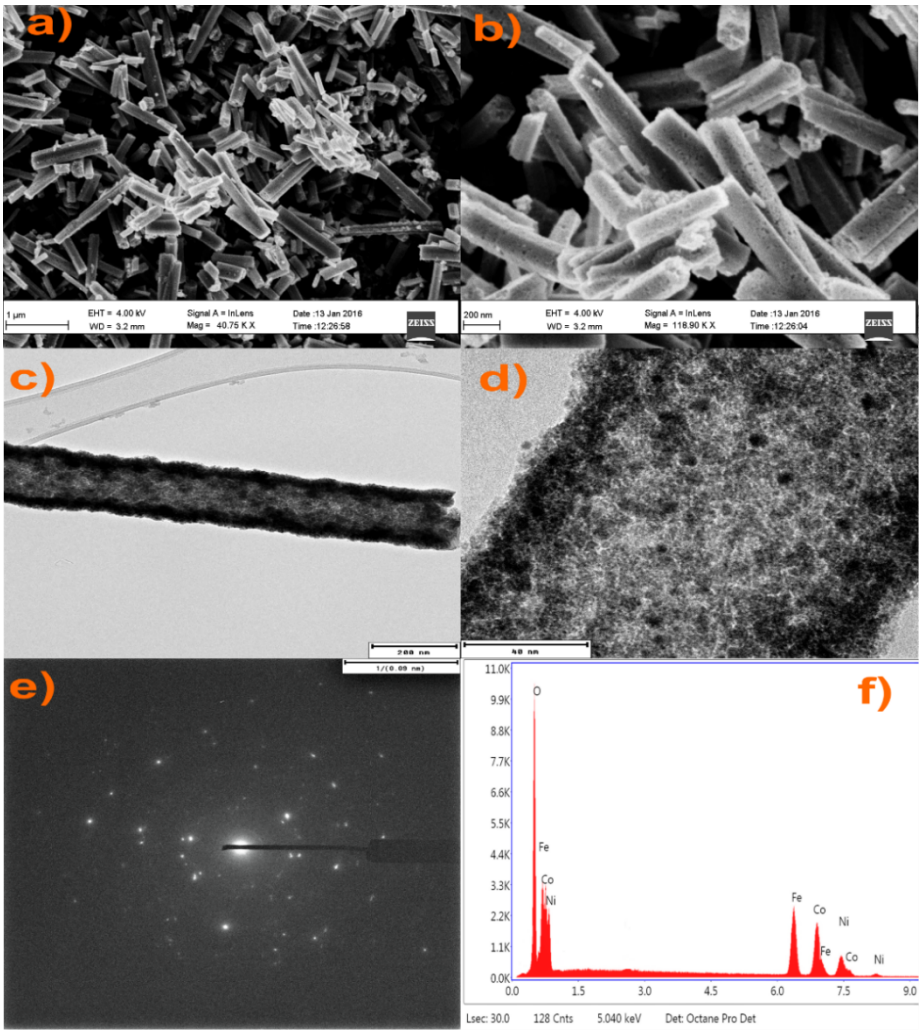

Figure 1 a) and B) FESEM image of ternary oxide nanorods synthesized by microwave method at various magnifications, c) and D) TEM image of single oxide nanorod e) selected area electron diffraction pattern f) EDX analysis of produced nanorods.

Figure 1.f shows the obtained EDX spectrum of the prepared $NiCoFeO_4$ nanorods, where several characteristic peaks for Ni, Co, Fe, and O. This confirms the successful formation of oxide nanorods by the microwave process. The elemental composition obtained from EDX analysis reveals that the atomic percentages of Ni, Co, Fe, and O are 9.76%, 10.1%, 12.08%, and 68.06%, respectively. As a result, their atomic ratio is approximately 1: 1: 1: 6.

X-ray diffraction patterns of $NiCoFeO_4$ nanorods synthesized via the microwave process is shown in Figure. 2.a. The peaks at 2θ values corresponding to 30.5°, 36°, 43.5°, 57.5°, and 63° can be indexed to (220), (311), (400), (511), and (440) crystal planes respectively. The XRD pattern shows the characteristic peak of ferrite material with the most intense peak (311), which confirms the formation of the cubic spinel structure. The X-ray diffraction pattern fits well with JCPDS card No. 42-1467, confirms the formation of $NiCoFeO_4$ nanorods with spinel structure. [13] [34]

Raman spectroscopy is employed for further structural and vibrational investigation of the prepared $NiCoFeO_4$ nanorods. The Raman spectrum of $NiCoFeO_4$ nanorods in Figure 2.b shows five strong Raman modes. Spinel structure has five Raman active modes ($A_{1g} + E_g + 3F_{2g}$).[35] [36] The peaks at 320, 580 and 750 cm^{-1} correspond to the Eg, T_{2g}, A_{1g}, and modes of ($NiCoFeO_4$) nanorods, respectively. The Raman peaks at 950 and 1020 could be assigned to two-phonon (2P) TO + LO and 2LO modes of NiO phase.[37][38]

XPS is employed to characterize the surface chemistry and chemical state of $NiCoFeO_4$ nanorods. The XPS survey spectrum in Figure 2.c indicates the presence of Fe, Co, Ni, and O in the $NiCoFeO_4$ nanorods. All the binding energies in the XPS spectra were calibrated for specimen charging with reference to the C 1s peak (set at 284.8 eV) and no impurities were detected. Co 2p XPS peaks corresponding to $Co_{2p3/2}$ and $Co_{2p1/2}$ are observed at the binding energies of 779.7 and 795.9 eV, respectively, suggesting the formation of Co^{2+}. Two major peaks centered at 855.4 and 872.5 eV are assigned to $Ni_{2p3/2}$ and $Ni_{2p1/2}$, respectively, confirming the Ni^{2+} oxidation state $NiCoFeO_4$ nanorods. The strong peak located at 710.04 eV corresponds to the $Fe_{2p3/2}$ of the Fe^{3+} cations. The peak at 530 corresponds to O 1s oxidation state that is related to the metal–oxygen bonds.[34,39,40]

Surface area is a very crucial property to evaluate supercapacitor electrode material. Figure 2.d shows the N_2 adsorption/ desorption isotherm for the $NiCoFeO_4$ nanorods. Adsorption/ desorption isotherms are classified according to IUPAC. According to IUPAC classification, the obtained N_2 adsorption/ desorption isotherm is of type IV.[41] Hysteresis loop is the main characteristic of type IV adsorption/ desorption isotherm. This hysteresis loop is associated with capillary condensation occur in the mesopores and this phenomenon appears when adsorption and desorption curves do not coincide. These features confirm the mesoporous structure of the prepared $NiCoFeO_4$ nanorods.[41] Actual surface area $NiCoFeO_4$ nanorods can be obtained from BET analysis of type IV isotherms. The surface area resulted from multipoint BET is 118.4 m^2/g. The mesoporous nature $NiCoFeO_4$ nanorods with high surface area enhance and facilitates ion and electron diffusion and transport at the electrolyte-electrode interface, which results in higher electrochemical performance.

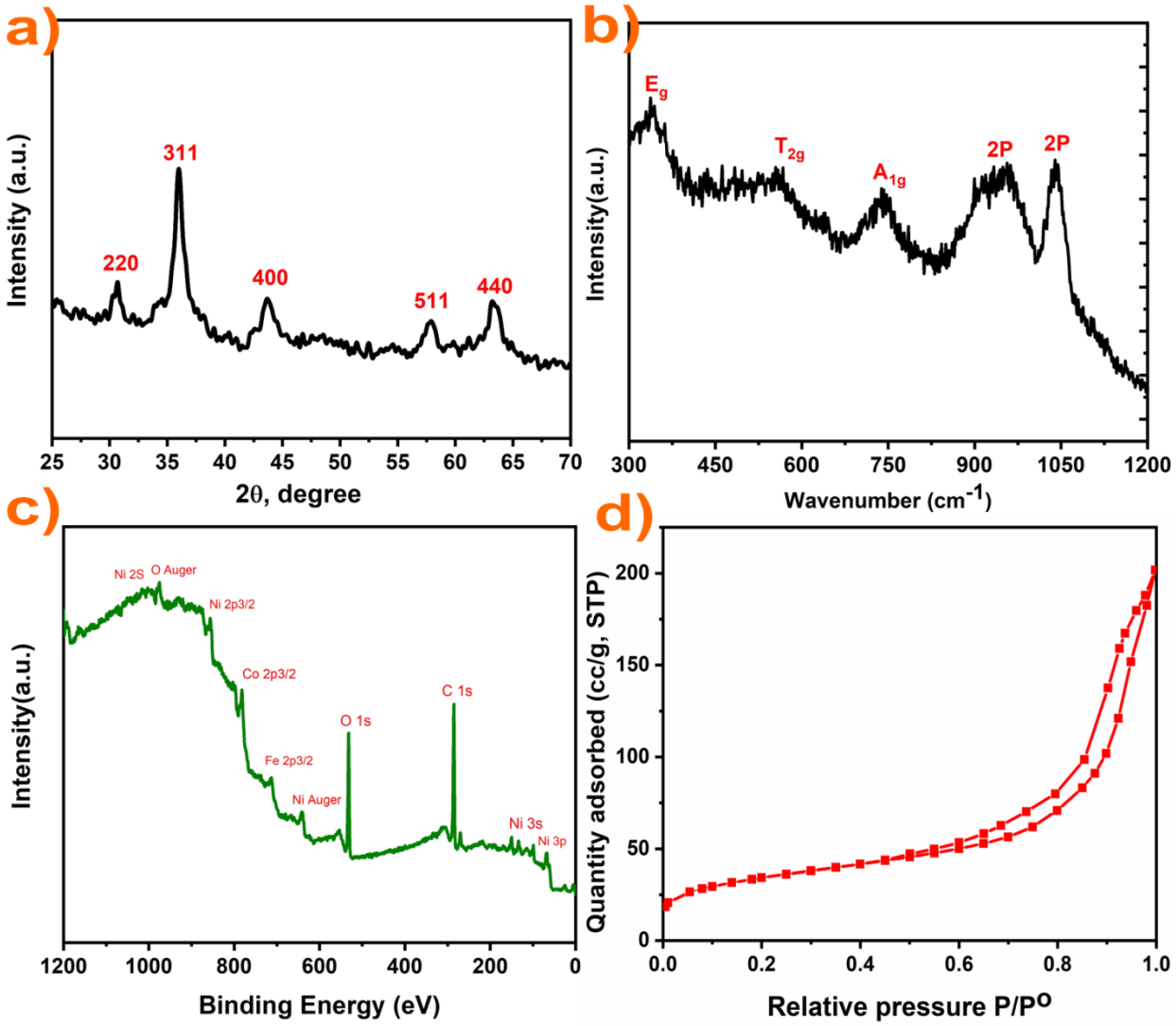

Figure 2 a) X-ray diffraction pattern of $NiCoFeO_4$ oxide nanorods, b) Raman spectrum of $NiCoFeO_4$ oxide nanorods, c) XPS spectrum of $NiCoFeO_4$ oxide nanorods, and e) N_2 adsorption/desorption isotherm of $NiCoFeO_4$ oxide nanorods.

Electrochemical characterization

The electrochemical supercapacitive performance of $NiCoFeO_4$ nanorods was investigated through CV and GCD measurements. The CV curves of $NiCoFeO_4$ nanorods in Figure 3.a were carried out in the potential range of 0 – 0.45 VSCE at various scan rates in 6 M KOH. The CV curves have two peaks appear at 0.38 V and 0.05 V for the oxidation and reduction processes, respectively which prove faradic-type capacitive features. The peak current density (I_p, A/g) of $NiCoFeO_4$ nanorod increases as a function of scan rate. The specific capacitance (C_{sp}) calculated from CV measurements is dependent on scan rate. The maximum C_{sp} (1234 F/g) is obtained at 1 mV/sec (the slowest scan rate), while C_{sp} is 495 F/g at 100 mV/sec. This is due to the presence of a large ohmic resistance at high scan rates. In addition, at high scan rate, the electrolyte ions do not possess enough time to diffuse through the electrode where the faradaic reactions occur.[42] This behavior proposes that there are parts of the electrode surface inaccessible at high charging/discharging rates.[43] Therefore, a slower scan rate is an effective approach for electrochemical energy stored in the $NiCoFeO_4$ supercapacitor. Figure 3.a displays the pairs of redox peaks corresponding to Co^{3+}/Co^{2+}, Ni^{3+}/Ni^{2+}, and Fe^{2+}/Fe^{3+} redox transitions. The redox peaks of Co^{3+}/Co^{2+}, Ni^{3+}/Ni^{2+}, and Fe^{2+}/Fe^{3+} imply to be merging together because of their comparable standard electrode potentials.[44,7,6,45] The capacitive behavior of $NiCoFeO_4$ nanorods can be related to the presence of three redox systems. The redox reactions could proceed according to eqn (7), (8) and (9), respectively [46]

For Ni^{3+}/Ni^{2+}

$$Ni(OH)_2 + OH^- \longleftrightarrow NiOOH + H_2O + e \qquad \text{Equation 7}$$

For Co^{3+}/Co^{2+}

$$Co(OH)_2 + OH^- \longleftrightarrow CoOOH + H_2O + e \qquad \text{Equation 8}$$

For Fe^{2+}/Fe^{3+}

$$Fe(OH)_2 + OH^- \longleftrightarrow FeOOH + H_2O + e \qquad \text{Equation 9}$$

The peaks of oxidation and reduction shift transfers to more anodic and cathodic values with the increase in scan rate. Also, the peak-to-peak separation ($\Delta E_{p\text{-}p}$), the potential difference between anodic and cathodic peaks, increases when increasing the scan rate, which may be due to the insufficient ions access to the electrode surface.[47] At high scan rates, electrolyte ions do not have sufficient time to reach the electrode surface, creating an unavoidable overpotential associated with an increase in the internal diffusion resistance. [48] The fast-interfacial kinetics causes anodic peak current ($I_{p,a}$) to be increased from 2.363 to 60.14 (A/g) as scan rate increases.[43]

Another precise method for investigating the electrochemical performance of pseudo-capacitance supercapacitors is galvanostatic charge/discharge (GCD) measurement.[42] Figure 3.c displays the GCD curves recorded for $NiCoFeO_4$ nanorods in 6 M KOH. GCD curves of $NiCoFeO_4$ show deviations from linearity due to its pseudocapacitive nature while GCD curves of carbon exhibiting a semi-triangular shape due to pure electric double layer capacitance. the $NiCoFeO_4$ electrode displays higher charging and discharging times upon decreasing current density which leads to higher values of specific capacitance (Figure 3.d). For example, on decreasing the current density from 11 A/g to 1 A/g, C_{sp} increases from 458 to 1263 F/g. Moreover, Figure 3.d also shows that the columbic efficiency (η%) reaches 89% at 5 A/g current density, after which the columbic efficiency becomes nearly constant (85%). Table 1 depicts the supercapacitive performance parameters, including C_{sp} for $NiCoFeO_4$ nanorods and some ternary and quaternary TM ferrites. It should be noted that $NiCoFeO_4$ has an excellent C_{sp} in comparison to those of the previously investigated materials.

Table 1: Specific capacitance for various ternary mixed-metal oxides.

Electrode Materials	Specific Capacitance (F/g)	Ref.
Ni-Zn-Co oxide nanowire arrays	776	[49]
Mn-Ni-Co oxide nanowire array	638	[50]
NiSe/NF	1790	[51]
$Ni(OH)_2$/Ni	1228	[52]
WS_2NPs–encapsulated CTs	337	[53]
porous tubular C/MoS_2	210	[54]
$MnCoFeO_4$	670	[55]
$NiCoFe_2O_4$	50	[14]
$NiCuFe_2O_4$	44	
$CuCoFe_2O$	76.9	
Mesoporous $CuCo_2O_4$ nanowires Nano casting from silica	1210	[56]
$NiCoFeO_4$ nanorods	1263	This work

Figure 3 (a) CV curves of $NiCoFeO_4$ nanorods in 0–0.45 V.SCE potential range in 6 M KOH electrolyte at various scan rates, (b) specific capacitance dependence on scan rate, c) $NiCoFeO_4$ nanorods galvanostatic charge/discharge curves and (d) the calculated C_{sp} and η% in 0–0.45 V.SCE potential range of in 6 M KOH electrolyte at different current densities.

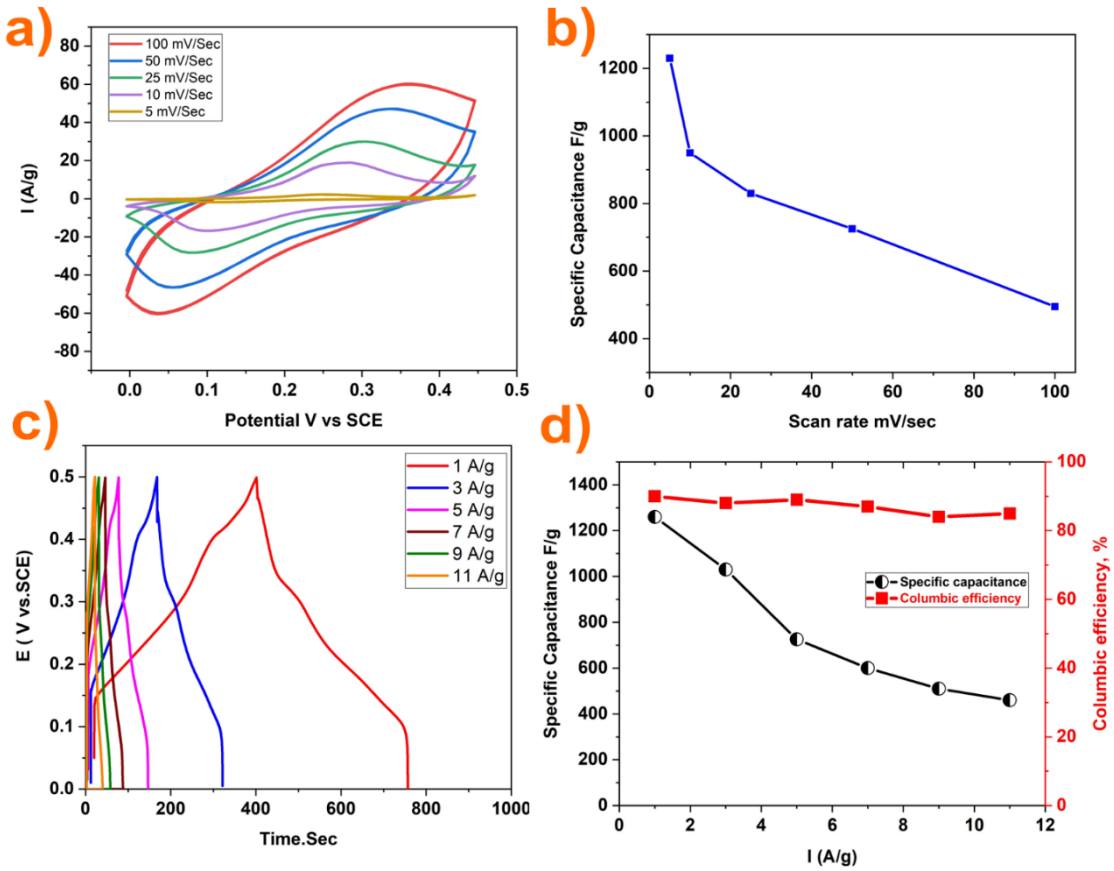

3.2.2. Cycling stability

Cycling stability (capacitance retention (%)) is another essential tool that regulates the durability of supercapacitors. Figure 4.b shows the capacitance retention (%) of the $NiCoFeO_4$ nanorods recorded during 2000 consecutive GCD cycles at 11 A/g current density. The capacitance preserves 97.2 % after 2000 GCD cycles, indicating excellent long-term stability. The synergistic effects of the transition metal oxide could provide excellent stability of $NiCoFeO_4$ nanorods.[42]

EIS is an effective method carried out to investigate the electrode/electrolyte interface of supercapacitors.[57] EIS offers information about electrode internal resistant and electrode-electrolyte charge transfer resistance.[58] EIS spectra of $NiCoFeO_4$ nanorods is shown in Figure 4.a. Figure 4.a shows a depressed high-frequency semicircle and a low-frequency inclined straight line. These features indicate that the electrolyte/electrode redox reactions are limited by the mass transfer process, i.e. diffusion-controlled reactions.[43]

Based on EIS results, an equivalent circuit (EC) is suggested. The employed EC model is composed of R1 representing the solution resistance in series with the time constant (CR_2W), which describes the depressed semicircle. C is the double layer capacitance, R2 stands for the charge transfer resistance caused by the faradaic process and Warburg impedance W is the frequency-dependent electrolyte diffusion resistance.[59] Table 2 lists the EIS parameters obtained for $NiCoFeO_4$ nanorods. Solution resistance (R1) remained nearly constant after 2000 GCD cycles where it changed very slightly from 1.82 □ to 3.57 □. Charge transfer resistance (R2) suffered a little increase reaching a maximum value of only 0.29 □. The Warburg value W increased from 40.1 □ $s^{0.5}$ to 52.7 □ $s^{0.5}$ indicating the occurrence of a slight decrease in the diffusion rate of electrolyte ions arriving at the electrode surface over the long-term use. Accordingly, EIS confirms that $NiCoFeO_4$ nanorods have excellent long-term stability with insignificant change in its ESR.

Table 2: EIS parameters calculated for $NiCoFeO_4$ nanorods electrode before and after 2000 cycles GCD

	Fresh electrode	After 2000 cycle
R1	1.82	3.57
C	3.59	1.15
R2	0.031	0.29
W	40.1	52.7

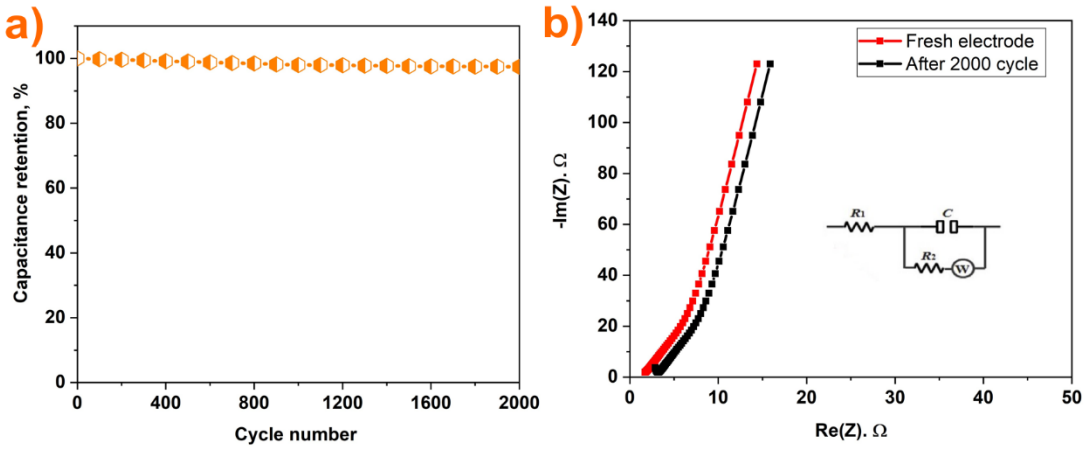

Figure 4 (a) $NiCoFeO_4$ nanorods cycling stability curves, and (b) $NiCoFeO_4$ nanorods Nyquist spectrum obtained before and after 2000 GCD cycles.

Device measurements

To identify potential practical applications of $NiCoFeO_4$ nanorods as an electrode material for an asymmetric supercapacitor device. The asymmetric device was prepared using the $NiCoFeO_4$ nanorods as a positive electrode and AC as a negative electrode. The electrochemical properties of the asymmetric supercapacitor cell were measured and presented in Figure 5.a–d. Figure 5.a presents the CV curves of the $NiCoFeO_4$//AC asymmetric supercapacitor at different scan rates from 10 to 200 mV/sec over 0 to 1.6 V potential range of in 6 M KOH electrolyte. The redox peaks were still noticeable in all CV curves indicating the faradaic-type behavior of the $NiCoFeO_4$//AC asymmetric supercapacitor. Figure 5.b shows charge-discharge curves of the asymmetric supercapacitor at different current densities of 1, 3, 5, 7 and 9 A/g. The nonlinear charge-discharge profile confirmed the contribution of Faradaic-type performance from $NiCoFeO_4$ nanorods. Figure 5.c presents the cycling performance of the asymmetric device. Only 6 % capacity decay and a high coulombic efficiency of 95.5 % were observed after 4000 cycles of charging and discharging of the $NiCoFeO_4$ //AC device at a current density of 9 A/g, indicating the remarkable reversibility and stability of the device.

The relationship between energy density (E_d) and power density (P_d) was determined using a Ragone plot, as shown in Figure 5.d. The E_d and P_d were calculated based on the total weight of the two electrodes. The Ragone plot in Figure 5.d presents E_d vs. P_d for the $NiCoFeO_4$//AC asymmetric supercapacitor. The highest E_d was 32 W h/kg at a power density of 0.97 kW/kg and the highest P_d of 10 kW/kg at an E_d of 9.8 W h/kg. Such high output energies and power densities were highly competitive compared to those of the recently-reported ternary oxides based asymmetric supercapacitor devices as summarized in Table 3.

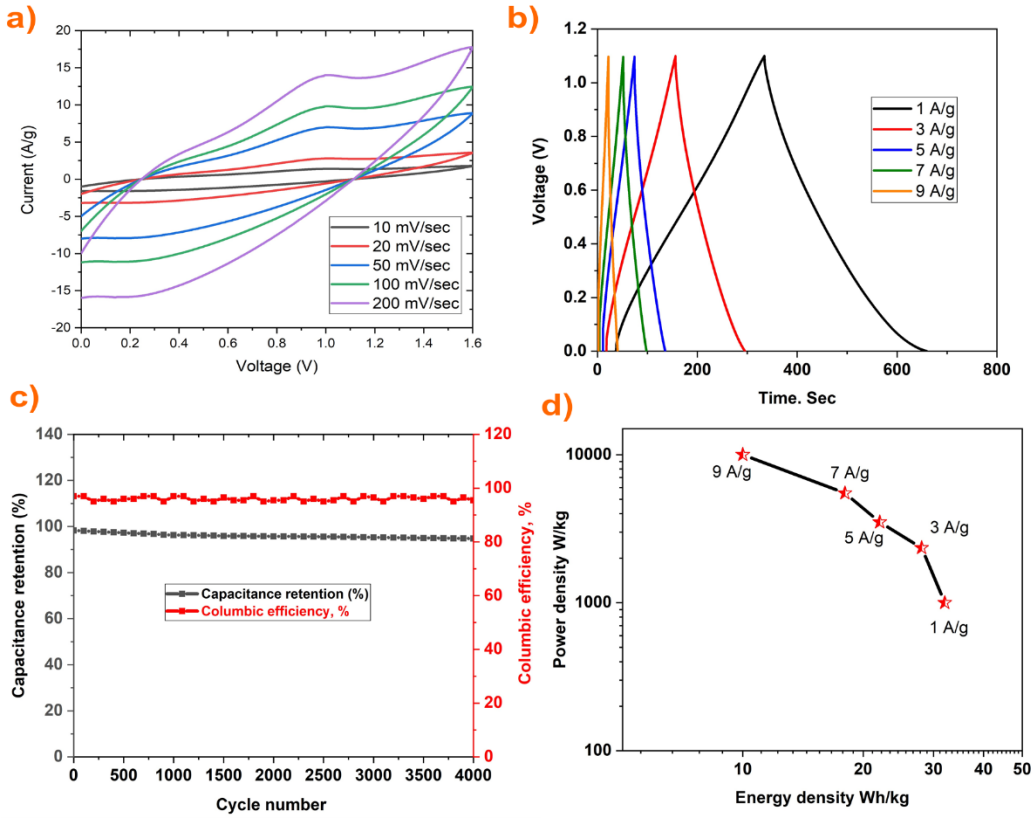

Figure 5 characterization of $NiCoFeO_4$//AC asymmetric device: (a) CV curves at various scan rates, (b) GCD curves at various current densities, (c) cycling performance at a current density of 9 A/g, and (d) Ragone plot correlating E_d and P_d of the device.

Table 3: Main features of relevant ternary oxides supercapacitors.

Material	E_d (Wh/kg)	P_d(W/kg)	Ref
$MnCoFeO_4$	3.15	2250	[55]
$MnCo_2O_4$	10.04	5000.2	[60]
$NiCoFe_2O_4$	4.79	1426.23	[14]
$NiCuFe_2O_4$	4.62	1001.29	[14]
$CuCoFe_2O_4$	3.53	198.5	[61]
$CuCoFe_2O$	7.9	1711.95	[14]
$NiCoFeO_4$	32	10000	This work

Conclusions

This work presented a facile synthesis of $NiCoFeO_4$ ternary mixed oxide nanorods as determined via FE-SEM, TEM, EDX, XRD, Raman, and XPS analysis. $NiCoFeO_4$ nanorods supercapacitive performance was carried out in three-electrode cell setup in 6.0 M KOH using CV and GCD measurements. $NiCoFeO_4$ nanorods exhibit a pseudocapacitive behavior during CV with a high specific capacitance of 1234 F/g at a scan rate of 5 mV/sec. The GCD curves also achieved a specific capacitance of 1263 F/g at a current density of 1 A/g. $NiCoFeO_4$ nanorods asymmetric supercapacitor device showed excellent cycling stability with capacitance retention reaching 94 % even after 4000 cycles. $NiCoFeO_4$ nanorods asymmetric supercapacitor device also showed 10 KW/kg power density and 32 Wh/kg energy density of at 9 A/g charging current density. The outstanding supercapacitive performance and stability of $NiCoFeO_4$ nanorods can be attributed to unique morphology, high surface area, and synergetic effect of mixed transition metal oxide.

Acknowledgment

Erasmus Mundus scholarship is acknowledged for making this work available.

Funding

This research has no external funding.

Conflicts of Interest

There are no conflicts of interest.

Data Availability

The raw/processed data required to reproduce these findings cannot be shared at this time as the data also forms part of an ongoing study.

References

1 C. Liu, F. Li, L.-P. Ma and H.-M. Cheng, *Adv. Mater.*, 2010, **22**, E28–E62.

2 P. Simon and Y. Gogotsi, *Nat. Mater.*, 2008, **7**, 845–854.

3 N. Choudhary, C. Li, J. Moore, N. Nagaiah, L. Zhai, Y. Jung and J. Thomas, *Adv. Mater.*, 2017, **29**, 1605336.

4 L. Hao, X. Li and L. Zhi, *Adv. Mater.*, 2013, **25**, 3899–3904.

5 Y. Shabangoli, M. S. Rahmanifar, M. F. El-Kady, A. Noori, M. F. Mousavi and R. B. Kaner, *Energy Storage Mater.*, 2018, **11**, 282–293.

6 C. D. Lokhande, D. P. Dubal and O.-S. Joo, *Curr. Appl. Phys.*, 2011, **11**, 255–270.

7 C. Yuan, H. Bin Wu, Y. Xie and X. W. D. Lou, *Angew. Chemie Int. Ed.*, 2014, **53**, 1488–1504.

8 M. K. Zate, S. M. F. Shaikh, V. V. Jadhav, K. K. Tehare, S. S. Kolekar, R. S. Mane, M. Naushad, B. N. Pawar and K. N. Hui, *J. Anal. Appl. Pyrolysis*, 2015, **116**, 177–182.

9 S. S. Alaa Faid, Alejandro Oyarce Barnett, Frode Seland, *J. Electrochem. Soc.*, 2019, **166**, 1–33.

10 A. Faid, A. Oyarce Barnett, F. Seland, S. Sunde, A. Y. Faid, A. Oyarce Barnett, F. Seland and S. Sunde, *Catalysts*, 2018, **8**, 614.

11 D. H. Deng, H. Pang, J. M. Du, J. W. Deng, S. J. Li, J. Chen and J. S. Zhang, *Cryst. Res. Technol.*, 2012, **47**, 1032–1038.

12 B. Bhujun, M. T. T. Tan and A. S. Shanmugam, *Ceram. Int.*, 2016, **42**, 6457–6466.

13 B. Bhujun, M. T. T. Tan and A. S. Shanmugam, *Results Phys.*, 2017, **7**, 345–353.

14 B. Bhujun, M. T. T. Tan and A. S. Shanmugam, *Results Phys.*, 2017, **7**, 345–353.

15 P. Guo, Z. Li, S. Liu, J. Xue, G. Wu, H. Li and X. S. Zhao, *J. Mater. Sci.*, 2017, **52**, 5359–5365.

16 W. Wang, Q. Hao, W. Lei, X. Xia and X. Wang, *J. Power Sources*, 2014, **269**, 250–259.

17 J. L. Gunjakar, A. M. More, K. V. Gurav and C. D. Lokhande, *Appl. Surf. Sci.*, 2008, **254**, 5844–5848.

18 J.-J. Deng, J.-C. Deng, Z.-L. Liu, H.-R. Deng and B. Liu, *J. Mater. Sci.*, 2009, **44**, 2828–2835.

19 D. Carriazo, J. Patiño, M. C. Gutiérrez, M. L. Ferrer and F. del Monte, *RSC Adv.*, 2013, **3**, 13690.

20 H. Wang, C. M. B. Holt, Z. Li, X. Tan, B. S. Amirkhiz, Z. Xu, B. C. Olsen, T. Stephenson and D. Mitlin, *Nano Res.*, 2012, **5**, 605–617.

21 A.-H. Lu and F. Schüth, *Adv. Mater.*, 2006, **18**, 1793–1805.

22 A. Taguchi and F. Schüth, *Microporous Mesoporous Mater.*, 2005, **77**, 1–45.

23 S. Komarneni, M. C. D'Arrigo, C. Leonelli, G. C. Pellacani and H. Katsuki, *J. Am. Ceram. Soc.*, 2005, **81**, 3041–3043.

24 S. Komarneni, R. Roy and Q. H. Li, *Mater. Res. Bull.*, 1992, **27**, 1393–1405.

25 C. O. Kappe, *Angew. Chemie Int. Ed.*, 2004, **43**, 6250–6284.

26 I. Bilecka and M. Niederberger, *Nanoscale*, 2010, **2**, 1358.

27 W.-W. Wang, *Mater. Chem. Phys.*, 2008, **108**, 227–231.

28 X. Gu, W. Zhu, C. Jia, R. Zhao, W. Schmidt and Y. Wang, *Chem. Commun.*, 2011, **47**, 5337.

29 S.-W. Cao, Y.-J. Zhu, G.-F. Cheng and Y.-H. Huang, *J. Hazard. Mater.*, 2009, **171**, 431–435.

30 B. C. Kim, M. Rajesh, H. S. Jang, K. H. Yu, S. J. Kim, S. Y. Park and C. J. Raj, *J. Alloys Compd.*, 2016, **674**, 376–383.

31 D. Zhao, F. Hu, A. Umar and X. Wu, *New J. Chem.*, 2018, **42**, 7399–7406.

32 A. K. Yedluri and H. J. Kim, *RSC Adv.*, 2019, **9**, 1115–1122.

33 F. Yuan, Y. Ni, L. Zhang, S. Yuan and J. Wei, *J. Mater. Chem. A*, 2013, **1**, 8438.

34 J. Zhao, C. Li, Q. Zhang, J. Zhang, X. Wang, J. Sun, J. Wang, J. Xie, Z. Lin, Z. Li, W. Lu, C. Lu and Y. Yao, *Nano Res.*, 2018, **11**, 1775–1786.

35 M. De, G. Bera and H. S. Tewari, *Int. J. Math. Phys. Sci. Res. ISSN*, 2015, **3**, 71–76.

36 P. R. Graves, C. Johnston and J. J. Campaniello, *Mater. Res. Bull.*, 1988, **23**, 1651–1660.

37 I. Sildos, I. Steins, A. Kuzmin, J. Grabis, M. Pärs and N. Mironova-Ulmane, *J. Phys. Conf. Ser.*, 2007, **93**, 012039.

38 G. George and S. Anandhan, *RSC Adv.*, 2014, **4**, 62009–62020.

39 H. Xiao, M. Yu, Y. Li, X. Lu and W. Qiu, *Chem. Eng. J.*, 2018, **352**, 996–1003.

40 T. Wang, W. Xu and H. Wang, *Electrochim. Acta*, 2017, **257**, 118–127.

41 K. S. W. Sing, *Pure Appl. Chem.*, 1985, **57**, 603–619.

42 T. van Ree, Y. Wu, C. Li, Y. Zhu, L. Zhou and X. Liu, *Metal oxides in supercapacitors*, Elsevier Inc., 2018.

43 A. E. Elkholy, F. El-Taib Heakal and N. K. Allam, *Electrochim. Acta*, 2019, **296**, 59–68.

44 G. Xu, Z. Zhang, X. Qi, X. Ren, S. Liu, Q. Chen, Z. Huang and J. Zhong, *Ceram. Int.*, 2018, **44**, 120–127.

45 Y. Zhang, L. Li, H. Su, W. Huang and X. Dong, *J. Mater. Chem. A*, 2015, **3**, 43–59.

46 D. Chen, Q. Wang, R. Wang and G. Shen, *J. Mater. Chem. A*, 2015, **3**, 10158–10173.

47 X. Tang, B. Tang, Z. Shang, W. Hu, D. Li, J. Qiu and Y. She, *Coatings*, 2018, **8**, 340.

48 I. Hussain, S. G. Mohamed, A. Ali, N. Abbas, S. M. Ammar and W. Al Zoubi, *J. Electroanal. Chem.*, 2019, **837**, 39–47.

49 W. Hu, H. Wei, Y. She, X. Tang, M. Zhou, Z. Zang, J. Du, C. Gao, Y. Guo and D. Bao, *J. Alloys Compd.*, 2017, **708**, 146–153.

50 L. Li, Y. Zhang, F. Shi, Y. Zhang, J. Zhang, C. Gu, X. Wang and J. Tu, *ACS Appl. Mater. Interfaces*, 2014, **6**, 18040–18047.

51 C. Tang, Z. Pu, Q. Liu, A. M. Asiri, X. Sun, Y. Luo and Y. He, *ChemElectroChem*, 2015, **2**, 1903–1907.

52 B. Hu, X. Qin, A. M. Asiri, K. A. Alamry, A. O. Al-Youbi and X. Sun, *Electrochim. Acta*, 2013, **107**, 339–342.

53 B. Hu, X. Qin, A. M. Asiri, K. A. Alamry, A. O. Al-Youbi and X. Sun, *Electrochem. commun.*, 2013, **28**, 75–78.

54 B. Hu, X. Qin, A. M. Asiri, K. A. Alamry, A. O. Al-Youbi and X. Sun, *Electrochim. Acta*, 2013, **100**, 24–28.

55 A. E. Elkholy, F. El-Taib Heakal and N. K. Allam, *RSC Adv.*, 2017, **7**, 51888–51895.

56 A. Pendashteh, S. E. Moosavifard, M. S. Rahmanifar, Y. Wang, M. F. El-Kady, R. B. Kaner and M. F. Mousavi, *Chem. Mater.*, 2015, **27**, 3919–3926.

57 A. D. Jagadale, V. S. Kumbhar, D. S. Dhawale and C. D. Lokhande, *Electrochim. Acta*, 2013, **98**, 32–38.

58 A. Rai, A. L. Sharma and A. K. Thakur, *Solid State Ionics*, 2014, **262**, 230–233.

59 J. Huang, *Electrochim. Acta*, 2018, **281**, 170–188.

60 S. Sahoo, K. K. Naik and C. S. Rout, *Nanotechnology*, 2015, **26**, 455401.

61 B. Bhujun, M. T. T. Tan and A. S. Shanmugam, *Ceram. Int.*, 2016, **42**, 6457–6466.